MIT Libraries | DSpace@MIT

MIT Open Access Articles

Modeling the point-spread function in helium-ion lithography

The MIT Faculty has made this article openly available. ***Please share*** how this access benefits you. Your story matters.

Citation: Winston, Donald et al. "Modeling the Point-Spread Function in Helium-Ion Lithography." Scanning 34.2 (2012): 121–128.

As Published: http://dx.doi.org/10.1002/sca.20290

Publisher: Wiley Blackwell

Persistent URL: http://hdl.handle.net/1721.1/74145

Version: Author's final manuscript: final author's manuscript post peer review, without publisher's formatting or copy editing

Terms of use: Creative Commons Attribution-Noncommercial-Share Alike 3.0

Massachusetts Institute of Technology

Preprint *in press*, Scanning
(journal website: http://dx.doi.org/10.1002/sca.20290).

Modeling the point-spread function in helium-ion lithography

D. Winston[a,b,*], J. Ferrera[a], L. Battistella[a], A. E. Vladár[b], K. K. Berggren[a,c]
[a]*Massachusetts Institute of Technology, Cambridge, MA, US*
[b]*National Institute of Standards and Technology, Gaithersburg, MD, US*
[c]*Technical University of Delft, Delft, NL*

*Corresponding author:
Donald Winston
77 Massachusetts Ave
Building 36, Suite 213
Cambridge, MA 02139
dwinston@mit.edu

Keywords

Monte Carlo modeling, Focused Ion Beam, Metrology, Electron-beam lithography

Abstract

We present here a hybrid approach to modeling helium-ion lithography that combines the power and ease-of-use of the Stopping and Range of Ions in Matter (SRIM) software with the results of recent work simulating secondary electron (SE) yield in helium-ion microscopy. This approach traces along SRIM-produced helium-ion trajectories, generating and simulating trajectories for SEs using a Monte Carlo method. We found, both through simulation and experiment, that the spatial distribution of energy deposition in a resist as a function of radial distance from beam incidence, i.e. the point spread function, is not simply a sum of Gauss functions.

Introduction

The helium-ion microscope (HIM) holds promise as a scanning-beam tool of high resolution for both microscopy and fabrication. For microscopy, the HIM is being developed to extract surface detail at a large depth of focus (Postek and Vladár 2008). For fabrication, the HIM has been used for exposure of resist in lithography (Sidorkin *et al.* 2009; Winston *et al.* 2009), beam-induced deposition (Sanford *et al.* 2009), and milling (Bell *et al.* 2009; Scipioni *et al.* 2010).

For a scanning-beam system, knowledge of the point-spread function (PSF), or spatial distribution of energy deposition, is useful for model-based measurement of critical dimensions (Villarrubia and Ding 2009) and for proximity-effect correction in fabrication (Chang 1975). One can also derive expectations for resolution and contrast of a particular scanning-beam system from a PSF and compare these with similarly-derived expectations of other scanning-beam systems.

A simulator to estimate the PSF for lithography with the HIM has not yet been reported. The IONiSE simulator (Ramachandra *et al.* 2009) was recently developed to understand SE yield for microscopy with the HIM, and the EnvisION simulator (Smith *et al.* 2010) extended results from IONiSE for beam-induced deposition with the HIM. This paper presents, based on results from IONiSE, a simulator to estimate the PSF for lithography with the HIM. First, we explain the model we used. Next, we describe the implementation of our model and present its results. Then, we present the method and results of an experiment to validate the model. Finally, we compare our model to the experimental PSF and discuss the utility of the model.

Model

SRIM (Ziegler *et al.* 2008) is a popular, industry-standard tool for simulating the trajectories of incident ions in a target sample. However, SRIM does not simulate the trajectories of secondary electrons (SEs) produced by ion-sample interactions. SEs are responsible for exposure of resist and thus figure prominently in modeling of electron-beam lithography (Joy 1983) and proton-beam lithography (Udalagama *et al.* 2009). We present here a hybrid approach to modeling helium-ion lithography that combines the power and ease-of-use of SRIM with the results of recent work simulating SE yield in helium-ion microscopy (Ramachandra *et al.* 2009). This approach traces along SRIM-produced helium-ion trajectories, generating and simulating trajectories for these SEs using a Monte Carlo method (Ghanbari 1993; Joy 1995).

Figure 1 illustrates the procedure we followed for modeling. First, we obtained a set of ion trajectories via SRIM's "Collision Details" feature. The trajectories were piecewise-linear because SRIM uses a single-scattering model in which an ion loses energy without deflection between major elastic nuclear scattering events. Next, we generated the full set of SEs for all the ion trajectories. Then, we simulated the trajectories of the SEs. Finally, we returned the spatial distribution of energy deposited in the specimen.

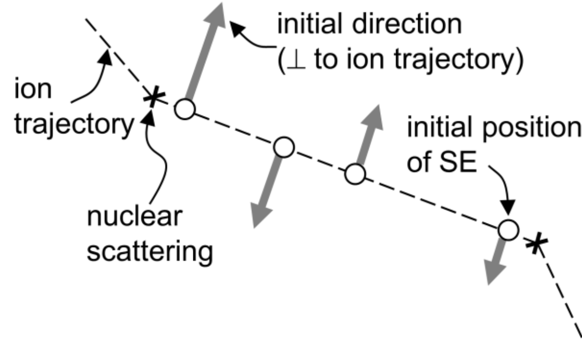

Figure 1: Schematic diagram of the generation of SEs along a leg (dotted line between nuclear scattering events) of a helium-ion trajectory. A Poisson process determines the initial positions (circles) of SEs along the leg. The length of a gray arrow represents the initial direction of a SE, projected onto the plane of the diagram. Choice of initial energy for a SE is discussed in the text.

The initial position, direction and energy of each SE were calculated as follows. Along each straight-line path of length s between scattering events, we initiated a Poisson process for SE generation with energy $(\partial E/\partial s) \times s$ available to the process, where $\partial E/\partial s$ was the average of the instantaneous electronic stopping powers recorded by SRIM at the locations of the scattering events bounding the s-path. To calculate $\partial E/\partial s$ for the s-path preceding the first scattering event, we used the instantaneous electronic stopping power calculated by SRIM for the resist material at the ion landing energy. The arrival rate of generated SEs along a given path in a material was taken to be (Ramachandra *et al.* 2009)

$$\delta_{\mathrm{SE}} = -\left(1/\varepsilon\right) \times \frac{\partial E}{\partial s}, \qquad (1)$$

where ε is the effective energy required to produce an SE. The initial direction of an SE was uniformly random in the plane perpendicular to the ion trajectory at the point of generation of the SE. The initial energy of a generated SE was sampled from a Rayleigh distribution (Bertsekas and Tsitsiklis 2002)

$$f_R\left(r\right) = \frac{r}{\sigma^2} e^{-r^2/2\sigma^2},\ r \geq 0 \qquad (2)$$

of mean $\mu = \sigma\sqrt{\pi/2}$ such that (Joy 1995)

$$\mu \text{ [keV]} = \left(\frac{\lambda_{\mathrm{D}} \text{ [nm]} \times \rho \text{ [g/cm}^3\text{]}}{75} \right)^{\frac{1}{1.66}}, \tag{3}$$

where Equation 3 is the Kanaya-Okayama equation (Kanaya and Okayama 1972) rearranged to obtain an electron's energy μ given its effective escape depth λ_d, termed the effective diffusion length in (Ramachandra *et al.* 2009), in a material of density ρ.

We chose to use a Rayleigh distribution for the probability density function of the initial energy of a generated SE because (1) we model each generated SE as having two degrees of freedom in space, in the plane perpendicular to the ion trajectory, for the first leg of the SE trajectory; and (2) we model the vector component of energy along each degree of freedom, meaning the kinetic energy associated with the vector component of velocity along that degree of freedom, as a normally distributed random variable.[1]

We chose to use Equation 3 for its simplicity and semi-empirical basis as an inversion of the $R = E^n/C$ relation between electron range R (or effective escape depth (Joy 1995)) and energy E (Kanaya and Kawakatsu 1972; Ramachandra *et al.* 2009), where C is a function of the material, and our parameterization was that of (Joy 1995) with $n = 5/3$. Alternatives for obtaining R for ≲100 eV electrons include using $n = 1$ (Kanaya and Kawakatsu 1972); using $R = \int_{E_F}^{E} \left[1/\left(dE/ds \right) \right] dE$ with stopping power dE/ds ∝ $\mathrm{E}^{5/2}$, where $\mathrm{E_F}$ is the Fermi energy (Joy

[1] We assume that many events with varying distributions add to produce the magnitude of the energy along each degree of freedom, and by the law of large numbers a summation of random variables results in a normal random variable. Because we are interested in the scalar value of the energy, we want the vector magnitude of the sum of two normally distributed random variables. The distribution describing such a vector magnitude is a Rayleigh distribution, i.e. R ~ Rayleigh(σ) is a Rayleigh distribution if $R = \sqrt{X^2 + Y^2}$, where $X \sim N(0,\sigma^2)$ and $Y \sim N(0,\sigma^2)$ are two independent normal distributions.

and Luo 1989; Nieminen 1988; Tung *et al.* 1979); and using the $A/E^2 + B\sqrt{E}$ universal curve of Seah and Dench (Ando and Muray 1988; Schou 1988; Seah and Dench 1979). A further refinement may be to express λ_d as a function of R, e.g. $\lambda_d = R/(1+f(Z))$, where $f(Z)$ is some function of atomic number (Kanaya and Okayama 1972). Considering the plethora of options for estimating μ and the dearth of investigations of SE energy spectra of non-metal targets – particularly insulators such as HSQ – under controlled experimental conditions (Hasselkamp 1992), we chose Equation 3 as a starting point for including SE generation and tracking in modeling of helium ion lithography.

Because a Poisson process initiates a random number of to-be-tracked SEs over any given leg of an ion trajectory, μ is not necessarily equal to ε, and some of the energy $(\partial E/\partial s) \times s$ available for SE generation along that leg remains unassigned. We dissipate this remaining energy uniformly along the leg. Thus, some of the electronic stopping power does work that is spatially confined to the ion trajectory.

We used $\varepsilon = 60$ eV and $\lambda_d = 9.75$ Å for both hydrogen silsesquioxane (HSQ) resist and for silicon. We estimated these values from Table 1 in (Ramachandra *et al.* 2009) as the minimum value plus the half-range (for λ_d we ignored the value for lithium, 25 Å, as an outlier in the set). We used this method to determine ε and λ_d because (1) we wanted to derive our values from the tabulated values in (Ramachandra *et al.* 2009); (2) there are no values tabulated for any of the elements of HSQ, namely H, Si, and O; and (3) there is no apparent trend for the values of ε and λ_d as a function of atomic number.

The given values of ε and λ_d yielded $\mu = 90$ eV, which is greater than ε and greater than typical energies measured for emitted SEs from ion bombardment (Hasselkamp 1992). The effect of $\mu > \varepsilon$ was to bias SE generation toward the beginning of each trajectory leg. While the

impact of this bias on the shape of the PSF was unclear, the semi-empirical basis of Equation 3 was preferred to, for example, setting $\mu = \varepsilon$ without physical parameterization. Regarding μ being larger than typical emitted-SE energies, we partially attribute this discrepancy to energy loss in transport through the material and to vacuum, but acknowledge this limitation of our model.

Following SE generation, the SE trajectory was calculated using a Monte Carlo method developed previously for modeling electron-beam lithography (Ghanbari 1993), modified to use Joy and Luo's adjustment to the Bethe equation for stopping power (Joy and Luo 1989). Although we could model the production and tracking of multiple generations of SEs by parent SEs, here we only tracked ion-produced SEs because (1) expressions for inelastic cross-section and stopping power of electrons in Monte Carlo simulation are suspect at very low (≤ 50 eV) energies (Joy 1995) and (2) tracking more than one generation of SEs has no noticeable effect in simulation of the lithographic PSF for other light ions (Udalagama *et al.* 2009).

Model implementation and results

We have developed two software programs, one for PSF calculation and one for rapid visualization of particle trajectories. Both programs use the same physics as described in the previous section, and both process output from SRIM as input. Calculation of PSFs is not memory intensive, but must be performed with many thousands of particles, whereas visualization is more memory intensive, but requires only a few hundred particles; thus, we separated these tasks. One program focuses on energy dissipation, but does not keep track of particle trajectories, and the other program collects trajectory information for rapid visualization,

but does not track energy dissipation. Details about the implementation of these programs, and the programs themselves, are available from the authors upon request.

Figure 2 plots the PSF resulting from 100,000 helium ions at 30 keV landing energy, infinitesimal spot size, and zero convergence angle entering a 12-nm-thick layer of hydrogen silsesquioxane (HSQ) resist on bulk silicon. The number of trajectories was 100,000 to yield a small (< 1%) standard error in the PSF statistics, even though e.g. the dose-to-print for 30 keV helium ions in HSQ resist is only ~1,000 ions (Sidorkin *et al.* 2009; Winston *et al.* 2009). The HSQ was given a stoichiometry of 8 Si, 8 H and 12 O as per its cage structure (Yang and Chen 2002) and we assumed a non-annealed film, which had a density of 1.4 g/cm^3 (Courtot-Descharles *et al.* 1999). The instantaneous electronic stopping power at the point of incidence, calculated by SRIM, was 6.042 eV/Å. The bulk silicon was amorphous as per the limits of Monte Carlo modeling and had a density of 2.33 g/cm^3. Mesh grid size was 1 nm in the radial direction and 5 nm in the surface-normal direction.

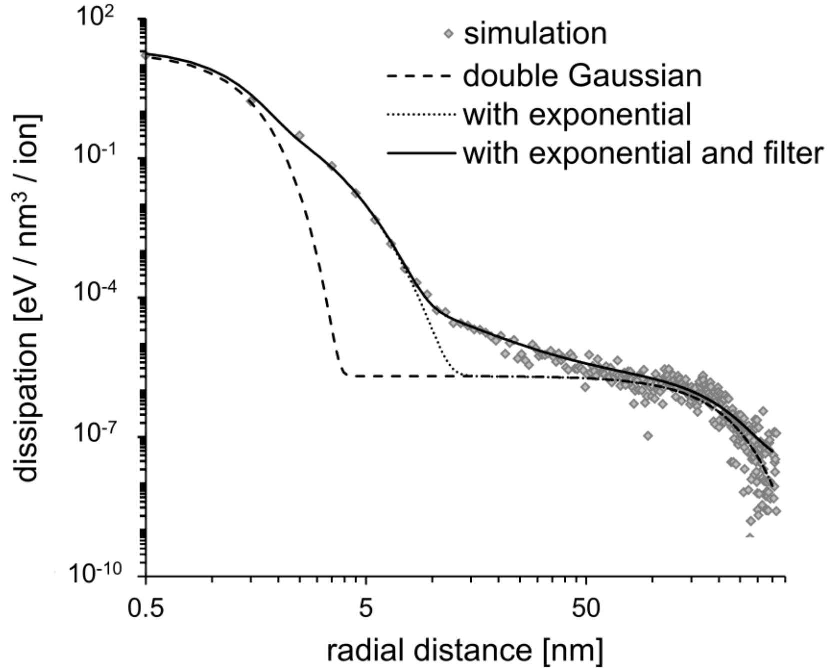

Figure 2: Simulated helium-ion PSF in 12-nm-thick HSQ on Si (diamonds), the fitting function of Equation 4 (solid line), a double Gaussian plus exponential function (dotted line), and a double Gaussian function (dashed line). We collected energy dissipated in mesh grid cells that ranged from 5 nm to 10 nm deep in the HSQ.

A function consisting of the sum of two Gaussians, an exponential term, and a term similar in appearance to the frequency response of a 2-pole low-pass filter,

$$A\left(\left(\frac{1}{\sigma_1^{\,2}}\right)e^{-\left(\frac{r}{\sigma_1}\right)^2}+\eta\left(\frac{1}{\sigma_2^{\,2}}\right)e^{-\left(\frac{r}{\sigma_2}\right)^2}\right)+Be^{-\frac{r}{r_\mathrm{e}}}+C\sqrt{\frac{1}{1+\left(r/r_\mathrm{f}\right)^4}} \tag{4}$$

was found to fit our simulation data, where $A \cong 18$, $\sigma_1 \cong 0.9$ nm, $\eta = 2.6\times10^{-3}$, $\sigma_2 = 150$ nm, $B = 5$, $r_\mathrm{e} = 0.8$ nm, $C = 2\times10^{-4}$, and $r_\mathrm{f} = 5$ nm. σ_1 indicates the beam spot size and the lateral extent of forward scattering, and σ_2 indicates the lateral extent of backscattering (Chang 1975). The exponential term may indicate Beer-Lambert-like absorption of SEs with r_e as the mean free path. The filter term is phenomenological; its physical meaning is unclear. Our fitting function is

overlaid on Figure 2 along with functions that successively remove the non-Gaussian terms, to highlight the role of these terms.

Figure 3(a) plots the trajectories of incident ions, incident electrons, and SEs on a side-view projection of the sample, 12 nm of HSQ on Si. A 30-keV helium-ion beam is compared to 30-keV, 10-keV, and 5-keV electron beams. Because our electron models assume non-relativistic energies, we do not include e.g. 100 keV as a plotted electron-beam landing energy. We tracked 200 30-keV helium ions. Because the critical dose for 30-keV electrons is approximately 5 times that of 30-keV helium ions (Sidorkin *et al.* 2009), we tracked proportionately more (1,000) 30-keV electrons. Similarly, in accordance with a $\log(E)/E$ scaling of stopping power for electrons (Joy and Luo 1989), we tracked 373 10-keV electrons and 202 5-keV electrons.

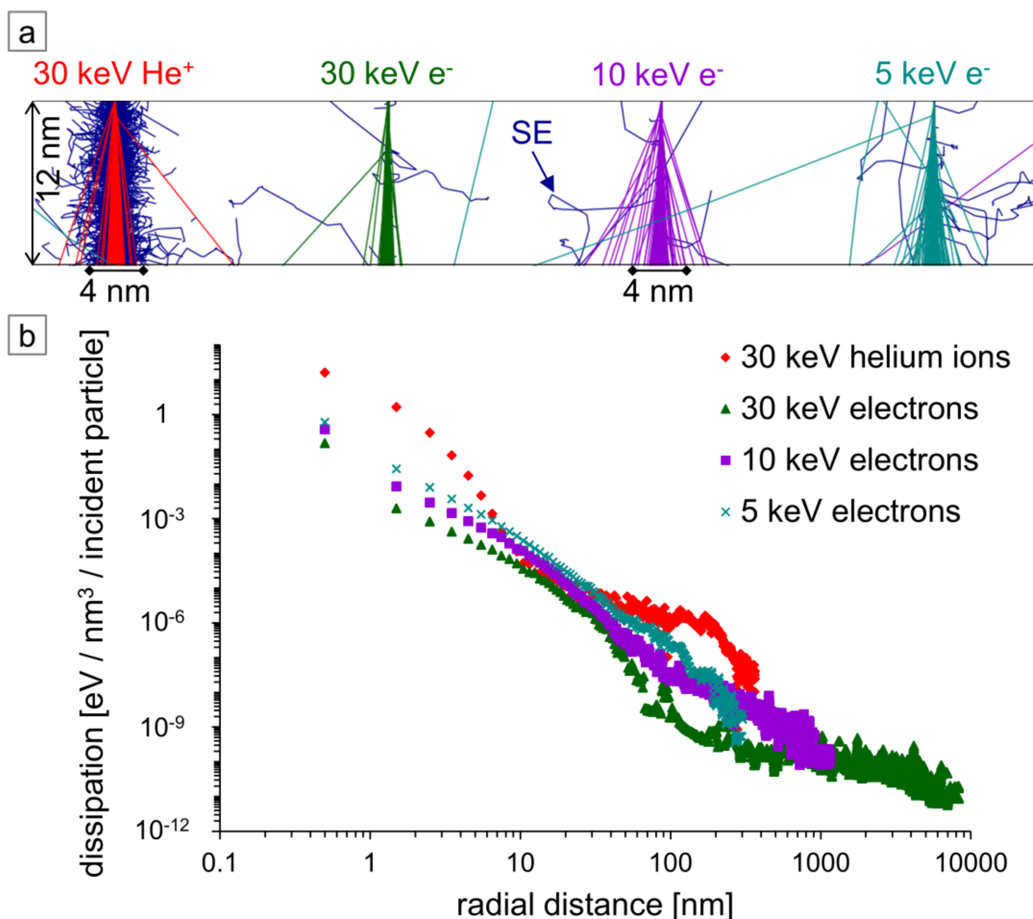

Figure 3: (a) Projection plot of trajectories for incident particles and their SEs, for helium-ion and electron beams, in 12-nm-thick HSQ on Si. To reduce calculation time and to focus attention on the short-range effects on feature size such as forward scattering and SE range, the Si layer is a 36-nm-thick membrane rather than a bulk substrate. The image is cropped at the base of the resist layer for clarity. (b) Simulated PSFs in 12-nm-thick HSQ on bulk Si for each of the four beams in (a): 30 keV He^+ (diamonds), 30 keV e^- (triangles), 10 keV e^- (squares), and 5 keV e^- (x's). We collected energy dissipated in mesh grid cells that ranged from 5 nm to 10 nm deep in the HSQ.

Figure 3(b) plots the PSFs of each of the four beams introduced in Figure 3(a). We tracked 100,000 ions for the PSF of 30-keV He^+ and we tracked 50,000 primary electrons for each of the PSFs of 30-keV e^-, 10-keV e^-, and 5-keV e^-. We applied a 5-nm-span moving average filter to each of the PSF plots beyond a radial distance of 100 nm, with the exception of the 30-keV electron PSF for which we applied a 20-nm-span filter, to smoothen statistical artifacts.

Experimental method and results

To measure the PSF, we performed a series of point exposures on a thin film of resist, developed the exposures using a high-contrast process, and estimated the widths of developed point exposures via top-down scanning electron microscopy (SEM). Although sub-10-nm metrology using a SE detector is difficult (Thoms and Macintyre 2010), this method allowed us to map out the PSF over several orders of magnitude in dose with minimal sample processing. Plotting inverse dose versus feature half-width obtains a non-normalized, non-parametric expression of the PSF (Menon *et al.* 2006; Rishton and Kern 1987).

Our procedures for sample preparation, pattern exposure, development, and metrology will now be described.

An approximately 10 by 10 mm silicon chip was prepared from a reclaimed test wafer of 76.2 mm (3 inch) diameter, 356-406 μm thickness, 1-100 Ω·cm resistivity, and <100> orientation. The wafer had been cleaned according to the RCA (Radio Corporation of America) cleaning, which is a removal of organic contaminants followed by a removal of the thin oxide layer and finished by a removal of metallic contaminants, but had been in storage for several weeks. Thus, we re-cleaned the wafer with O_2 plasma – 500 ml/min for 5 min in a microwave plasma system (PVA Tepla 300) – prior to cleaving the wafer with a diamond scribe to obtain our chip.

We diluted a commercially-available HSQ formulation (Dow Corning XR-1541-006) to obtain a thin film on our chip. First, we mixed 9 ml of methyl isobutyl ketone with 1 ml of the HSQ for a 0.6%-solids solution. Then, we placed a few drops of this solution on the bare Si chip for full wetting and spun the chip at 6,000 rpm for 30 seconds, with an initial angular

acceleration of 10,000 rpm/s. Finally, we measured the thickness of the film to be 12 nm by spectroscopic ellipsometry (Woollam M-2000 at 70° incidence).

Exposure was done on a HIM (Zeiss Orion Plus) connected to a pattern generator (Nabity NPGS v9). The HIM was operated with approximately 30 keV landing energy, 0.3 pA beam current, and a 5 μm beam-limiting aperture. Dwell times for point exposures varied from 10 μs to ~10 sec with an approximately 20% increase in dwell time from one exposure to the next. Spacing between point exposures was ≥ 300 nm to avoid dose overlap.

We developed the sample in an aqueous solution of 1 wt % NaOH and 4 wt % NaCl for 4 min at room temperature (unmeasured) (Yang and Berggren 2007). Next, we rinsed the sample for 30 sec in running deionized water to stop development. Then, we rinsed the sample for 30 sec in isopropyl alcohol to allow rapid drying. Finally, we dried the sample using a nitrogen gun.

Metrology used an in-lens FE-SEM (Hitachi S-5500) operating at 1 keV landing energy, 4.7 μA emission current, and 200 μm working distance. Due to the in-lens placement of the sample, we cleaved the chip around the patterned area to fit within a 4 mm × 9 mm sample chuck. 1 keV landing energy was chosen to limit beam interaction volume and enhance image contrast of surface detail for imaging the developed point exposures.

Figure 4 plots specified inverse dose versus measured half-width of the point-exposure features. A circular overlay tool in the ImageJ (Rasband 1997-2009) software was used to measure feature half-width in top-town SEM images. We also plot our model PSF, which was scaled to the experimental data by equating points at $r = 14.5$ nm, a tradeoff between metrological uncertainty in our experiment and statistical uncertainty in our simulation.

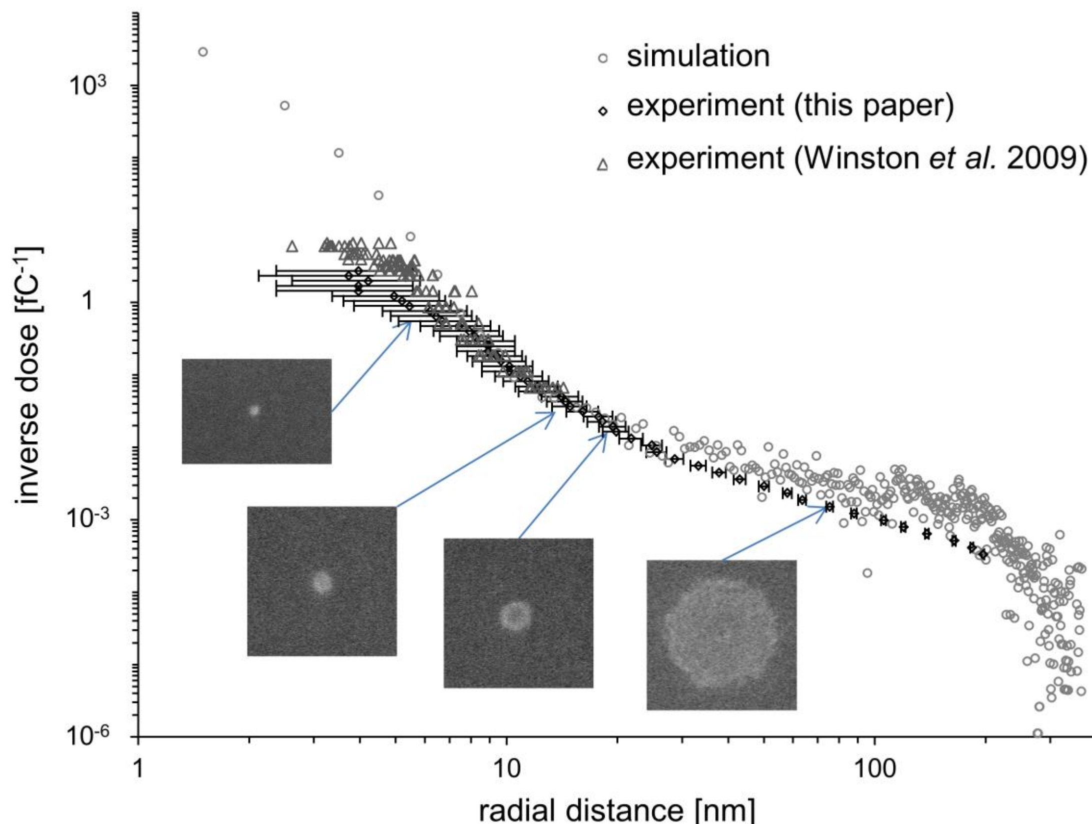

Figure 4: Inverse dose is plotted versus feature half-width (black diamonds); this plot is a (non-normalized) sampling of the PSF (Menon *et al.* 2006). Our lower bound on uncertainty in measuring width of features was 1.6 nm (half-width of black error bars), limited by beam spot size in our SEM. Our simulated PSF (light gray circles) was scaled to the experimental data by equating points at $r = 14.5$ nm. We include SEM images, each scaled to a width ≈ 200 nm, to illustrate the experimental method used to construct the plot. Also, we overlay experimental data on inverse dose versus feature half-width (dark gray triangles) presented in (Winston *et al.* 2009) that were obtained using 30-nm-thick HSQ but otherwise using the same conditions as the data introduced here.

Comparison of model with experiment, and discussion

For point doses greater than 100 fC (or 6.25×10^5 ions) for which experimental data was collected, simulation indicated a more rapid increase in the width of point-exposed features with dose than that observed by experiment (Figure 4). One hypothesis for this divergence is that beam-induced damage (Livengood *et al.* 2009) to the silicon at high fluence, for example

6.25×10^{18} ions/cm^2 for 100 fC focused to 10 nm^2, caused defects and nanobubbles to appear and thus decreased the mean free path of ions. This effect would not be accounted for by our simulation, which assumed an unblemished target for each incident ion. Also, our simulation may be inaccurate at long radial distances, perhaps due to inaccuracy in our stopping-power models at low energies.

For radial distances $r < 7$ nm, simulation indicated more process latitude than that observed by experiment (Figure 4), i.e. the width of sub-14-nm-diameter point-exposed features should vary less with dose than was observed. Our fit to the simulated PSF (Equation 4) and our interpretation of its parameter r_e as a mean free path suggests that reducing the parameter λ_d in our simulation could result in a smaller r_e and thus better overlap between experimental data and simulation. However, because the error bars of Figure 4 represent only a lower bound on metrological uncertainty, and because the experimental data only reach $r \gtrsim 4$ nm, the simulation may not be erroneous. Other metrological methods such as transmission electron microscopy (TEM) should be explored in future work to reduce uncertainty for small values of r.

One assumption implicit in Figure 4 is that the point spread function is radially symmetric. Our SEM images of point exposures show disks that appear roughly symmetrical, ignoring the stochastic nature of edge roughness and residues around the perimeters of the disks. We adjusted our beam to minimize stigmation prior to exposures.

Absent in Figure 4 is evidence of the backscattering terms η and σ_2 predicted by our fit to simulation (Equation 4). The experimental data for large r do not exhibit a rapid decay that would suggest a Gaussian term in the PSF, for backscattering. Given that the data for large r correspond to equivalent areal doses in excess of damage thresholds reported by (Livengood *et al.* 2009), we do not think that our predicted backscattering terms are observable with certainty

using the experimental method presented. However, our η and σ_2 parameters for backscattering were found to be consistent with simulation of the PSF without SE generation, i.e. spatially confined energy dissipation along each ion trajectory, which depends only on output from SRIM.

We do see a qualitative difference in appearance, via top-down SEM, between our point exposures at very high doses, i.e. doses much greater than the 1×10^{17} ions/cm^2 threshold of observed damage along the path of ion propagation reported by (Livengood *et al.* 2009), and those at smaller doses. Furthermore, the appearance of our point exposures at very high doses is consistent with the appearance of similarly dosed exposures on bare silicon. Figure 5 indicates that damage to the silicon may be causing deviation between our experimental and simulated PSF at high doses.

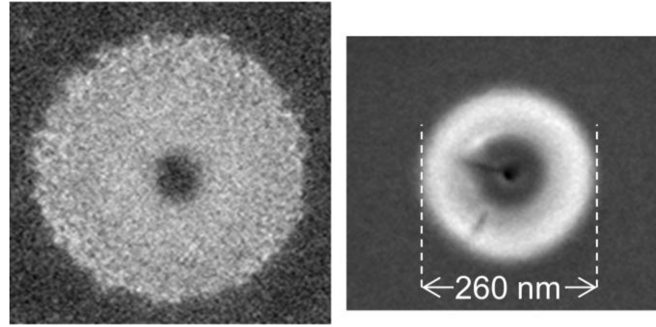

Figure 5: Scanning electron micrographs (same scale) at 1 keV and 0.2 mm working distance of *(left)* developed HSQ on Si and *(right)* bare Si, after 10-second point exposures of a 30 keV He^+ beam at 0.3 pA. Assuming a modest beam spot width of 3.5 nm, the effective ion fluence is 2×10^{20} ions/cm^2. The contrast of each image was normalized to an 8-bit range.

Figure 6 plots calculated dose contrast versus spatial frequency (reciprocal pitch) for exposure of a large-area grating using the simulation data of Figure 3(b). We define dose contrast K as

$$K = \frac{D_{\max} - D_{\min}}{D_{\max} + D_{\min}}, \quad (5)$$

where D_{max} is the dose delivered to the center of a line exposure near the center of the write field, and D_{min} is the dose delivered to a line equidistant from adjacent line exposures near the center of the write field. Experimentally, sub-10-nm pitch structures are difficult to obtain. Because Figure 6 predicts superior dose contrast for helium-ion exposure relative to electron exposure down to 6 nm pitch, helium-ion lithography appears to be a promising tool for dense patterning. Although Figure 6 suggests that ≥ 10 keV electrons are superior to helium ions for sub-6-nm pitch, the calculated dose contrast values do not account for the areal distribution of a beam at the surface of a resist, nor do they account for resist kinetics, all of which affect final patterning contrast. Thus, helium ions may be superior to ≤ 30 keV electrons for sub-6-nm pitch.

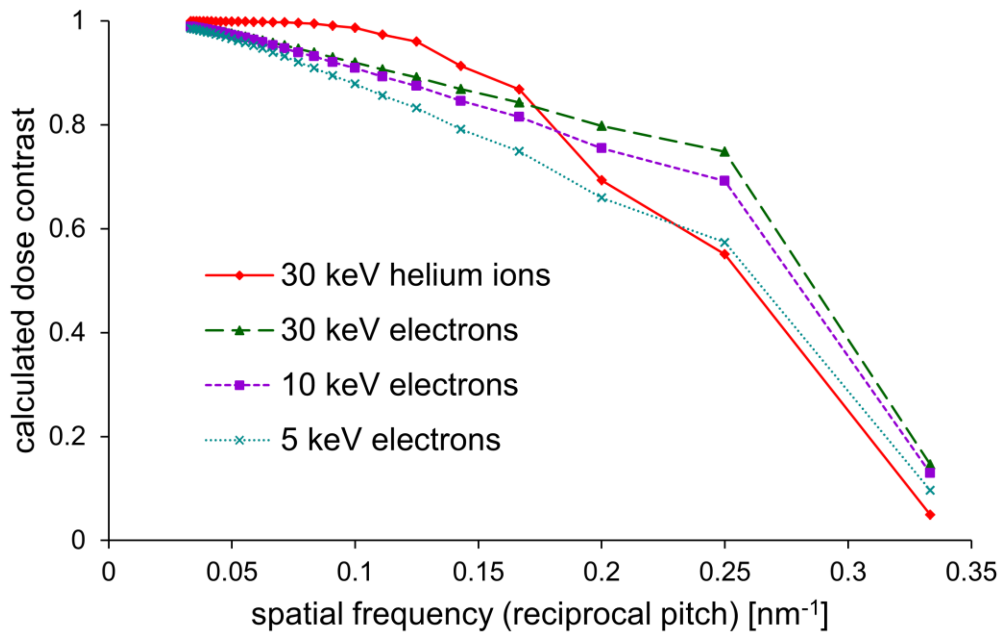

Figure 6: Calculated dose contrast versus reciprocal pitch for 30 keV He^+ and for three electron-beam energies. This plot used the simulation data of Figure 3(b) – values for dissipation versus radial distance were linearly interpolated within the range of data points and were taken as zero outside this range. The simulated exposure field was a 2 μm × 2 μm area of a grating of single-pixel lines, where both the pixel size and the step size along each line exposure was 1 nm.

Our simulation results may be sensitive to the assumption in our model that initial SE direction is perpendicular to the ion trajectory. In particular, because the direction of ion incidence is normal to the surface and because ion deflection due to nuclear scattering in a thin resist layer is typically small, the initial direction of most SEs is parallel to the surface. Thus, one may expect the average lateral range of SEs and thus of energy dissipation to be larger than if the initial SE direction was randomized. This bias implies that the simulated PSF in Figure 4 decays less rapidly with radial distance than it would if initial SE direction were randomized.

Conclusion

We have presented a model for the PSF of the helium-ion microscope and compared it to experimental measurement. We found good correspondence between our model and experiment in the mid-range of the PSF, and we have offered hypotheses for the discrepancies at the short- and long-range of the PSF. We also have produced software that is a first step toward combining the ease-of-use of SRIM with modeling of secondary electrons, an approach we hope will aid continued progress in understanding imaging and patterning with helium ions. Our model may be applied to various thicknesses of HSQ as well as to e.g. poly methyl methacrylate (PMMA) resist by simple changes to the small set of input parameters for our software – the resist's chemical formula, film density, and film thickness.

We found, both through simulation and experiment, that the spatial distribution of energy deposition in a resist as a function of radial distance from beam incidence, i.e. the PSF, is not simply a sum of Gauss functions. In particular, parts of the mid-range of the PSF exhibit exponential and power-law-like dependences. Future work will better elucidate a parametric formula, with a physical interpretation, for the PSF in helium-ion lithography.

Acknowledgements

The authors wish to acknowledge P. Kavuri for assistance with SEM and the CNST NanoFab at NIST. This work was sponsored by the SRC NRI, and D. Winston was partially supported by the NSF GRFP.

References

Ando M, Muray JJ. 1988. Spatial resolution limit for focused ion-beam lithography from secondary-electron energy measurements. J. Vac. Sci. Technol. B 6(3):986-8.

Bell DC, Lemme MC, Stern LA, Williams JR, Marcus CM. 2009. Precision cutting and patterning of graphene with helium ions. Nanotechnology 20(45):455301 (5 pp.).

Bertsekas DP, Tsitsiklis JN. 2002. Introduction to probability. Belmont, Mass.: Athena Scientific. 416 p.

Chang THP. 1975. Proximity effect in electron-beam lithography. J. Vac. Sci. Technol. 12(6):1271-1275.

Courtot-Descharles A, Pires F, Paillet P, Leray JL. 1999. Density functional theory applied to the calculation of dielectric constant of low-k materials. Microelectronics and Reliability 39(2):279-284.

Ghanbari RA. 1993. Physics and fabrication of quasi-one-dimensional conductors [Ph.D. thesis]. Cambridge: Massachusetts Institute of Technology.

Hasselkamp D. 1992. Kinetic electron emission from solid surfaces under ion bombardment. In: Hasselkamp D, Rothard H, Groeneveld K-O, Kemmler J, Varga P, Winter H, editors. Particle Induced Electron Emission II: Springer Berlin / Heidelberg. pp 1-95.

Joy DC. 1983. The spatial resolution limit of electron lithography. Microelectronic Engineering 1(2):103-119.

Joy DC. 1995. Monte Carlo modeling for electron microscopy and microanalysis. New York: Oxford University Press. 216 p.

Joy DC, Luo S. 1989. An empirical stopping power relationship for low-energy electrons. Scanning 11(4):176-80.

Kanaya K, Kawakatsu H. 1972. Secondary electron emission due to primary and backscattered electrons. Journal of Physics D: Applied Physics 5(9):1727.

Kanaya K, Okayama S. 1972. Penetration and energy-loss theory of electrons in solid targets. Journal of Physics D: Applied Physics 5(1):43.

Livengood R, Tan S, Greenzweig Y, Notte J, McVey S. 2009. Subsurface damage from helium ions as a function of dose, beam energy, and dose rate. J. Vac. Sci. Technol. B 27(6):3244-9.

Menon R, Gil D, Smith HI. 2006. Experimental characterization of focusing by high-numerical-aperture zone plates. J. Opt. Soc. Am. A 23(3):567-571.

Nieminen RM. 1988. Stopping power for low-energy electrons. Scanning Microscopy 2(4):1917-1926.

Postek MT, Vladár AE. 2008. Helium ion microscopy and its application to nanotechnology and nanometrology. Scanning 30(6):457-462.

Ramachandra R, Griffin B, Joy D. 2009. A model of secondary electron imaging in the helium ion scanning microscope. Ultramicroscopy 109(6):748-757.

Rasband WS. 1997-2009. ImageJ. http://rsb.info.nih.gov/ij/.

Rishton SA, Kern DP. 1987. Point exposure distribution measurements for proximity correction in electron beam lithography on a sub-100 nm scale. J. Vac. Sci. Technol. B 5:135-41.

Sanford CA, Stern L, Barriss L, Farkas L, DiManna M, Mello R, Maas DJ, Alkemade PFA. 2009. Beam induced deposition of platinum using a helium ion microscope. J. Vac. Sci. Technol. B 27(6):2660-2667.

Schou J. 1988. Secondary electron emission from solids by electron and proton bombardment. Scanning Microscopy 2(Copyright 1989, IEE):607-32.

Scipioni L, Ferranti DC, Smentkowski VS, Potyrailo RA. 2010. Fabrication and initial characterization of ultrahigh aspect ratio vias in gold using the helium ion microscope. J. Vac. Sci. Technol. B 28:C6P18-C6P23.

Seah MP, Dench WA. 1979. Quantitative electron spectroscopy of surfaces: a standard data base for electron inelastic mean free paths in solids. Surface and Interface Analysis 1(Copyright 1979, IEE):2-11.

Sidorkin V, van Veldhoven E, van der Drift E, Alkemade P, Salemink H, Maas D. 2009. Sub-10-nm nanolithography with a scanning helium beam. J. Vac. Sci. Technol. B 27(4):L18-L20.

Smith DA, Joy DC, Rack PD. 2010. Monte Carlo simulation of focused helium ion beam induced deposition. Nanotechnology 21(17):175302.

Thoms S, Macintyre DS. 2010. Linewidth metrology for sub-10-nm lithography. J. Vac. Sci. Technol. B 28:C6H6-C6H10.

Tung CJ, Ashley JC, Ritchie RH. 1979. Electron inelastic mean free paths and energy losses in solids II: Electron gas statistical model. Surface Science 81(2):427-439.

Udalagama C, Bettiol AA, Watt F. 2009. Stochastic spatial energy deposition profiles for MeV protons and keV electrons. Physical Review B 80(22):224107.

Villarrubia JS, Ding ZJ. 2009. Sensitivity of scanning electron microscope width measurements to model assumptions. J. Micro/Nanolith. MEMS MOEMS 8(3):033003-11.

Winston D, Cord BM, Ming B, Bell DC, DiNatale WF, Stern LA, Vladar AE, Postek MT, Mondol MK, Yang JKW, Berggren KK. 2009. Scanning-helium-ion-beam lithography with hydrogen silsesquioxane resist. J. Vac. Sci. Technol. B 27(6):2702-2706.

Yang C-C, Chen W-C. 2002. The structures and properties of hydrogen silsesquioxane (HSQ) films produced by thermal curing. Journal of Materials Chemistry 12(4):1138-1141.

Yang JKW, Berggren KK. 2007. Using high-contrast salty development of hydrogen silsesquioxane for sub-10-nm half-pitch lithography. J. Vac. Sci. Technol. B 25(6):2025-9.

Ziegler JF, Biersack JP, Ziegler MD. 2008. SRIM–The stopping and range of ions in matter. Chester, MD: SRIM Co.